JOURNAL OF GEOPHYSICAL RESEARCH, VOL. 105, NO. A5, PAGES 10,465–10,479, MAY 1, 2000

Improvement in the prediction of solar wind conditions using near-real time solar magnetic field updates

C. N. Arge

Cooperative Institute for Research in Environmental Sciences, University of Colorado and Space Environment Center, National Oceanic and Atmospheric Administration, Boulder

V. J. Pizzo

Space Environment Center, National Oceanic and Atmospheric Administration, Boulder, Colorado

Abstract. The Wang-Sheeley model is an empirical model that can predict the background solar wind speed and interplanetary magnetic field (IMF) polarity. We make a number of modifications to the basic technique that greatly improve the performance and reliability of the model. First, we establish a continuous empirical function that relates magnetic expansion factor to solar wind velocity at the source surface. Second, we propagate the wind from the source surface to the Earth using the assumption of radial streams and a simple scheme to account for their interactions. Third, we develop and apply a method for identifying and removing problematic magnetograms from the Wilcox Solar Observatory (WSO). Fourth, we correct WSO line-of-sight magnetograms for polar field strength modulation effects that result from the annual variation in the solar b angle. Fifth, we explore a number of techniques to optimize construction of daily updated synoptic maps from the WSO magnetograms. We report on a comprehensive statistical analysis comparing Wang-Sheeley model predictions with the WIND satellite data set during a 3-year period centered about the May 1996 solar minimum. The predicted and observed solar wind speeds have a statistically significant correlation ($\sim$0.4) and an average fractional deviation of 0.15. When a single (6-month) period with large data gaps is excluded from the comparison, the solar wind speed is correctly predicted to within 10-15%. The IMF polarity is correctly predicted $\sim$75% of the time. The solar wind prediction technique presented here has direct applications to space weather research and forecasting.

1. Introduction

During the Skylab era, large near-equatorial coronal holes were found to be associated with high-speed solar wind streams [*Nolte et al.*, 1976]. Using a current-free potential field model to map coronal magnetic field lines, *Levine et al.* [1977] found evidence for a correlation between open-field regions with small magnetic divergence and high-speed streams. This finding led Levine et al. to suggest that magnetic field divergence plays a "crucial physical role in the acceleration" of the solar wind. Using an empirical velocity equation that was a function of magnetic latitude, *Fry and Akasofu* [1987] simulated solar wind speed and interplanetary magnetic field (IMF) strength over two solar cycles and found that observed solar wind parameters could be reproduced for some coronal hole passages. *Wang and Sheeley* [1990] postulated the existence of an inverse correlation between magnetic expansion factor and solar wind speed. Using 22 years of photospheric field synoptic maps from Mount Wilson Solar Observatory and a potential field source-surface model [*Schatten et al.*, 1969], they calculated magnetic flux tube expansion rates and inferred solar wind speeds. Comparing their predicted 3-month running-average velocities with satellite observations, they obtained a statistically significant correlation coefficient (0.57) and concluded that fast solar wind emanates from regions with small magnetic divergence (e.g., from the central regions of coronal holes), and slow solar wind comes from regions with high magnetic divergence (e.g., boundaries of open-field regions overlying closed-field structures). However, their correlation strictly applied only to timescales on the order of months. In a subsequent work, *Wang and Sheeley* [1991] demonstrated that an inverse correlation between magnetic expansion factor and solar wind speed was consistent with some simple accelerations models involving Alfvén waves. Recently, *Wintoft and Lundstedt* [1997] found a correlation of 0.4 between observed and daily (Wang-Sheeley model) predicted so-

Paper number 1999JA900262.
0148-0227/00/1999JA900262$09.00

lar wind velocity. In an effort to further improve these predictions, *Wintoft and Lundstedt* [1997] combined an artificial neural network (ANN) with a potential field model. They trained the ANN on Wilcox Solar Observatory (WSO) data from solar cycle 21 and tested it on data from cycle 22. Their final model gave a velocity error of 90 km/s and a correlation of 0.58. They found inverse correlations between flux tube expansion and velocity, which ranged from over 0.5 for some years to less than 0.2 for other (e.g., 1985-1987 solar minimum). Successful efforts to predict the daily averaged IMF polarity at Earth have been recently reported by *Zhao and Hoeksema* [1995] and *Wang and Sheeley* [1995a].

Encouraged by the findings of *Wang and Sheeley* [1990, 1992, 1995a], *Wintoft and Lundstedt* [1997], and *Zhao and Hoeksema* [1995], we make a number of modifications to the original Wang-Sheeley (WS) model/prediction technique to further improve daily predictions of solar wind speed and IMF polarity at Earth. We test our modified approach by conducting a through investigation of the method over a 3-year period for which we have reasonably complete sets of daily solar magnetograms from WSO and corresponding in situ solar wind measurements from the WIND satellite (i.e., the 3-year period centered about the May 1996 solar minimum). The resulting predictions are subjected to rigorous statistical evaluation to assess how well the modified models perform, as compared to a traditional approach. We find that many subtle details about the handling of the magnetic data can significantly affect the performance of the model. When such details are carefully accounted for, the predictive reliability of the model is greatly improved. Advance predictions of the solar wind speed and IMF polarity can improve space weather forecasts and can provide more realistic boundary conditions for models of propagating solar wind disturbances.

2. Overview

In this paper, significant modifications are made to the prediction scheme originally employed by *Wang and Sheeley* [1990, 1992]. Improvements are made to both the quality and time resolution of the model's input data (i.e., synoptic maps of the photospheric field) and the method used to propagate the solar wind from the Sun to the Earth.

Two important changes are made to the WSO synoptic maps that are used as model input. The first concerns the rate at which the input data are updated. Whereas the traditional approach is to make predictions for the next solar rotation by using the synoptic map from the previous rotation, we update the synoptic maps daily (where possible) with new magnetograms and make predictions after each update. The second change to the model input is to enhance the quality of the synoptic maps by accounting for a number of problematic effects (e.g., east-west projection, solar b angle, and individual magnetogram quality) not currently included in the assembly of the maps. Uncorrected, these effects can produce erroneous results in the potential field source-surface (PFSS) calculation and therefore in the predictions.

The modeling process itself is modified in two ways. The first change is to establish a continuous empirical function that relates magnetic expansion factor to velocity. We use this empirical function to assign solar wind velocities at the source surface (given the magnetic expansion factors there), instead of at Earth, as in the work of *Wang and Sheeley* [1990, 1992]. The second change is to propagate the solar wind from the source surface to Earth using the assumption of radial solar wind streams and a simple scheme to account for their interactions. The PFSS code remains, however, the same as the original and is essentially the same as that currently used at WSO [*Hoeksema et al.*, 1982; *Zhao and Hoeksema*, 1994].

In section 3 we discuss methods for constructing the various types of synoptic maps from WSO magnetograms, including a detailed overview of the improvements to the data input. In particular, we highlight the important differences between the traditional synoptic maps (which we refer to as full-rotation maps) and the two types of daily updated synoptic maps used in this study. In section 4 we discuss the changes made to the original model in greater detail and outline the procedure for making predictions using a traditional approach and two modified versions of the model. We begin section 5 by selecting a subset of prediction results from our 3-year study, which illustrate the advantages and disadvantages of the three different prediction techniques. In the remainder of section 5, we undertake a rigorous statistical comparison of 3 years' worth of velocity and IMF predictions produced by each prediction method with WIND satellite observations. We summarize our findings in section 6.

3. Input to the Model

We highlight here the important differences between the traditional (i.e., full-rotation) synoptic maps and the daily updated maps, and we outline the general procedure for constructing them from WSO daily magnetograms.

3.1. Full-Rotation Synoptic Maps

One or two solar magnetograms are taken of the Sun each day at WSO. These low-resolution magnetograms extend 110° in longitude (centered about the Sun's central meridian) and ±14.5/15.0 in sine latitude. The precision of the individual magnetic field measurements are of the order of 5 μT [*Hoeksema*, 1984]. Upon interpolation onto Carrington coordinates, each magnetogram consists of 23×30 individual cells 5° in longitudinal width and 1/15 sine latitude in height. Because the Sun rotates ~13° per day as viewed from Earth,

magnetograms taken on consecutive days differ in their central meridian longitudes by ~10° to 15° (depending on the exact time of observation). Synoptic maps are constructed from daily magnetograms by overlaying them and using a weighted mean for overlapping regions. The weighting factor is a function of longitudinal distance and is sharply peaked at the location of the Sun's central meridian at the time of observation (see *Hoeksema* [1984] for further details). Each cell on a synoptic map can be, in principle, composed of up to ~16 individual observations weighted together (assuming there are no gaps in the observations) by the time the following (i.e., western) edges of subsequent magnetograms have rotated beyond the longitude of each cell. In practice, weather, instrument problems, and other factors limit the number of overlapping regions to fewer than 16. We define a full-rotation synoptic map as one whose leading (i.e., eastern) edge begins at some arbitrarily chosen initial Carrington longitude and that is no longer capable of being updated (i.e., the following edges of new magnetograms have rotated beyond the starting longitude). A full-rotation map is not complete until ~8 days after the starting Carrington longitude first appears within a magnetogram, because it takes ~8 days for the following edges of the daily magnetograms to rotate beyond it. We adopt the standard starting and ending Carrington longitudes of 0° and 360°, respectively, for all of our full-rotation synoptic maps.

3.2. Daily Updated Synoptic Maps

Synoptic maps that constitute the most recent 360° of observations and that begin with the leading edge of the most recent magnetogram are referred to as daily updated synoptic maps. These maps are normally composed of observations from portions of two different Carrington rotations (CRs). Unlike full-rotation maps the line-of-sight magnetic field values of the last 110° of a daily updated synoptic map are made up of progressively fewer averaged magnetograms. In fact, the most recent 10° to 15° of longitude added to the leading edges of these maps are often composed of observations from only one magnetogram. An advantage of a daily updated map (over a full-rotation map) is that the part of the map directed towards Earth consists of the most recent magnetic observations available, especially east of the Sun's central meridian. However, because the most recent magnetic data on the map are also based on the fewest number of observations, daily updated maps are much more sensitive to the quality of the individual magnetograms and are especially susceptible to projection effects east of the Sun's central meridian. For instance, the measured line-of-sight strength of a radially directed magnet field line located on the Sun's equator but 55° east (or west) of its central meridian is about a factor of 2 smaller than its true value. In the northern and southern corners of magnetograms the projection effects are even worse.

3.3. Modifications to the Daily Updated Synoptic Maps

We attempt to compensate for the above mentioned drawbacks in the daily updated maps through careful treatment of the individual magnetograms before they are assembled into synoptic maps.

3.3.1. Problematic magnetograms. To identify and minimize the influence of problematic magnetograms, we developed a scheme to evaluate the quality of each magnetogram beyond that already routinely applied at WSO. Three properties of the polar field data from both the northern and southern hemispheres (i.e., the magnetic data with sine latitudes of ±14.5/15.0) are used to evaluate the quality of each magnetogram. The average magnetic field $\langle B \rangle$ of each pole is calculated, along with the corresponding standard deviations σ_B of each $\langle B \rangle$, and the magnitude of the maximum spread (i.e., $|B_{\max} - B_{\min}|$) for each polar field. These three factors are compared with corresponding properties from a preselected reference set of 62 "good" magnetograms. For example, plotted in Figure 1 are the polar field values located at sine latitudes ±14.5/15.0 of a WSO magnetogram of very good quality. The reference magnetograms were selected from 1109 WSO magnetograms taken over a nearly 4-year time period (approximately late 1993 to late 1997) and include only those magnetograms with standard deviations of less than 40 μT for both north and south polar fields. A numerical quality factor Q is obtained for each pole by inserting these data into the following empirical equation:

$$Q = \sqrt{\left(\frac{\langle B \rangle - \langle B_{\rm ref} \rangle}{\langle \sigma \rangle_{B(\rm ref)}}\right)^2 + \left(\frac{\sigma_B}{\sigma_{B(\rm ref)}}\right)^2} \times \left(\frac{|B_{max} - B_{min}|}{\langle \sigma \rangle_{B(\rm ref)}}\right). \quad (1)$$

Here $\langle B_{\rm ref} \rangle$ is the average of the reference set's 62 individually averaged polar magnetic field strengths, $\sigma_{B(\rm ref)}$ is the corresponding standard deviation, and $\langle \sigma \rangle_{B(\rm ref)}$ is the average of the reference set's standard deviations. Magnetograms with both north and south Q factors less than 6.5 are accepted for inclusion in the daily updated synoptic maps. Magnetograms with one or both polar Q values greater than 6.5 are considered problematic. Because the extreme east and west edges of the magnetograms are often the source of the problem, 5° of data at both ends of the magnetogram are removed. The Q factor is then recalculated, and if both Q factors then fall below a value of 6.5, the longitudinally truncated magnetogram is used in the construction of the synoptic maps. If the Q factor remains above a value of 6.5 for either pole, an additional 5° of data from both edges are removed. This procedure is repeated until the reduced magnetogram's polar Q factors either fall below a value of 6.5 or more than 25° are cut from both ends of the magnetogram. In the latter case, the entire magnetogram is discarded. Roughly 12% of the magnetograms are not used for this reason. About 41% of

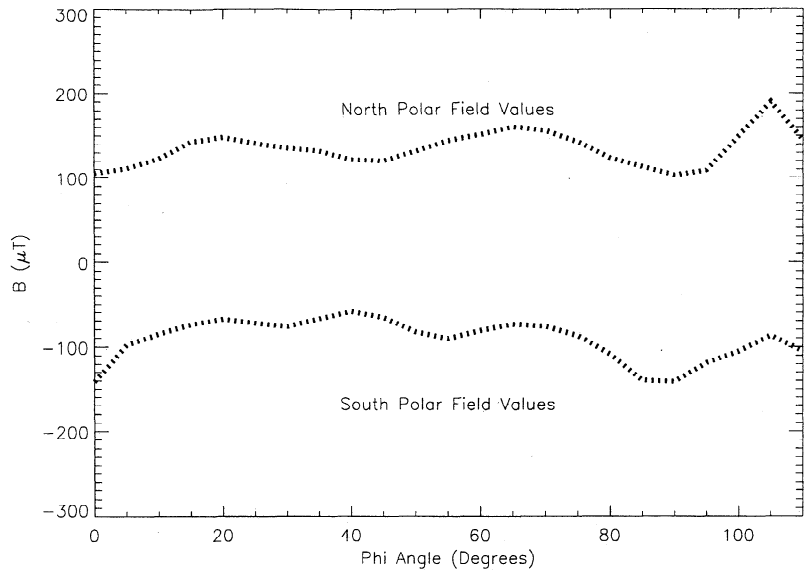

Figure 1. Example of a good Wilcox Solar Observatory (WSO) magnetogram (No. 5324). Plotted are the polar magnetic field values located at sine latitudes $\pm 14.5/15.0$.

the magnetograms are trimmed but less than 9% more than 15°. In Figure 2, we plot the polar field values of a magnetogram that is of very poor quality.

3.3.2. Projection effects. The WSO magnetograph records the line-of-sight (LOS) component of the solar photospheric magnetic field $B(B_r, B_\theta, B_\phi)$. Expressed in terms of the components of the actual field, the LOS magnetic field B_l is

$$B_l = B_r \sin\theta \cos(\phi - \phi_o) + \\ + B_\theta \cos\theta \cos(\phi - \phi_o) - B_\phi \sin(\phi - \phi_o), \quad (2)$$

where ϕ_o is the Carrington longitude of the Sun's central meridian at the time of observation and θ is the colatitude. Observational evidence [*Wang and Sheeley*, 1992; *Zhao and Hoeksema*, 1993] suggests that the solar magnetic field is nearly radial at the photosphere and therefore both $B_\theta \approx 0$ and $B_\phi \approx 0$. The LOS magnetic field data (B_l) should thus be corrected first for projection effects and then converted to the radial component of the potential field. Setting B_θ and B_ϕ to zero greatly simplifies (2):

$$B_l = B_r \sin\theta \cos(\phi - \phi_o). \quad (3)$$

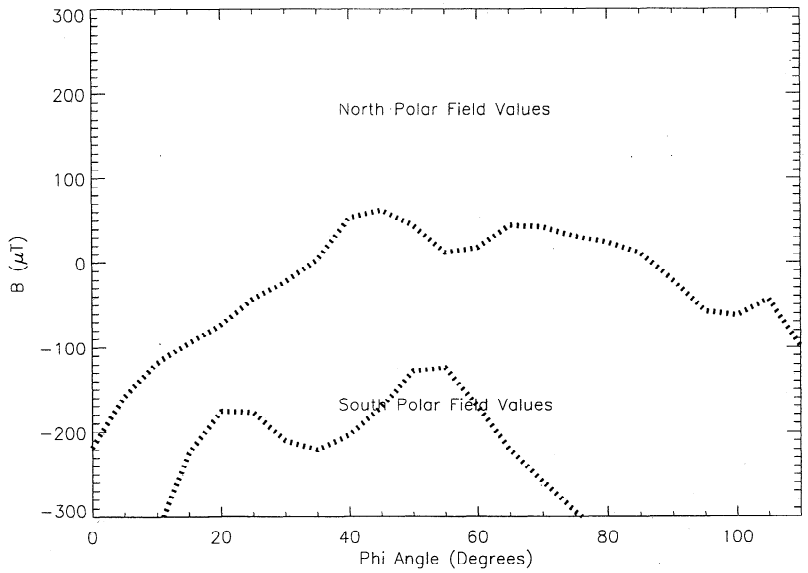

Figure 2. Example of an extremely bad WSO (No. 5332) magnetogram. Note the lack of uniformity in the polar field values compared with those in Figure 1.

Now B_r may be easily solved in terms of B_l. To do this, we first correct each magnetogram for longitudinal projection effects by dividing by $\cos(\phi - \phi_o)$, and then we adjust for latitudinal projection. This latter step is complicated by the time-varying tilt of the Sun's rotation axis as viewed from Earth (i.e., the solar b angle). We discuss this complication in the next section.

3.3.3. Corrections to the polar fields and the annual variation of the solar b angle. The global nature of the PFSS model makes it sensitive to the strengths of the polar magnetic fields, which are difficult to measure accurately. Determinations of the polar fields are further complicated by the 7.25° inclination of the Sun's rotation axis with respect to the ecliptic. When the solar b angle is +7.25°, the magnetic pole located in the Sun's northern hemisphere is observed much better from Earth than is the magnetic pole in the southern hemisphere; half a year later, when b = -7.25° the converse is true. Consequently, for a large fraction of a year, one of the Sun's magnetic poles is poorly measured.

This dilemma is illustrated in Figure 3, which plots both the northernmost and southernmost (i.e., sine latitudes ± 14.5/15.0) uncorrected average polar field strengths as a function of time (1994 to 1997) for those WSO magnetograms having solar b angles greater than | 5° |. (Only magnetic field measurements within 20° longitude of the Sun's central meridian are used to calculate the average polar field strengths.) As seen in Figure 3, when a particular hemisphere of the Sun is directed maximally toward the Earth, there is a spread of ~100-150 μT in the polar field values; however, the spread is larger (up to 200 μT) in the hemisphere directed away from the Earth.

We account for this difficulty by applying solar b angle corrections to the polar fields of each new magnetogram. Specifically, the corrections are made at sine latitudes ±14.5/15.0 (≈ ±75°) and ±13.5/15.0 (≈ ±64°). We fit a second-order polynomial to the most reliable corrected data at each of these polar latitudes (i.e., only data from magnetograms for which $b \geq +5.0°$ in the north and $b \leq -5°$ in the south) to approximate their

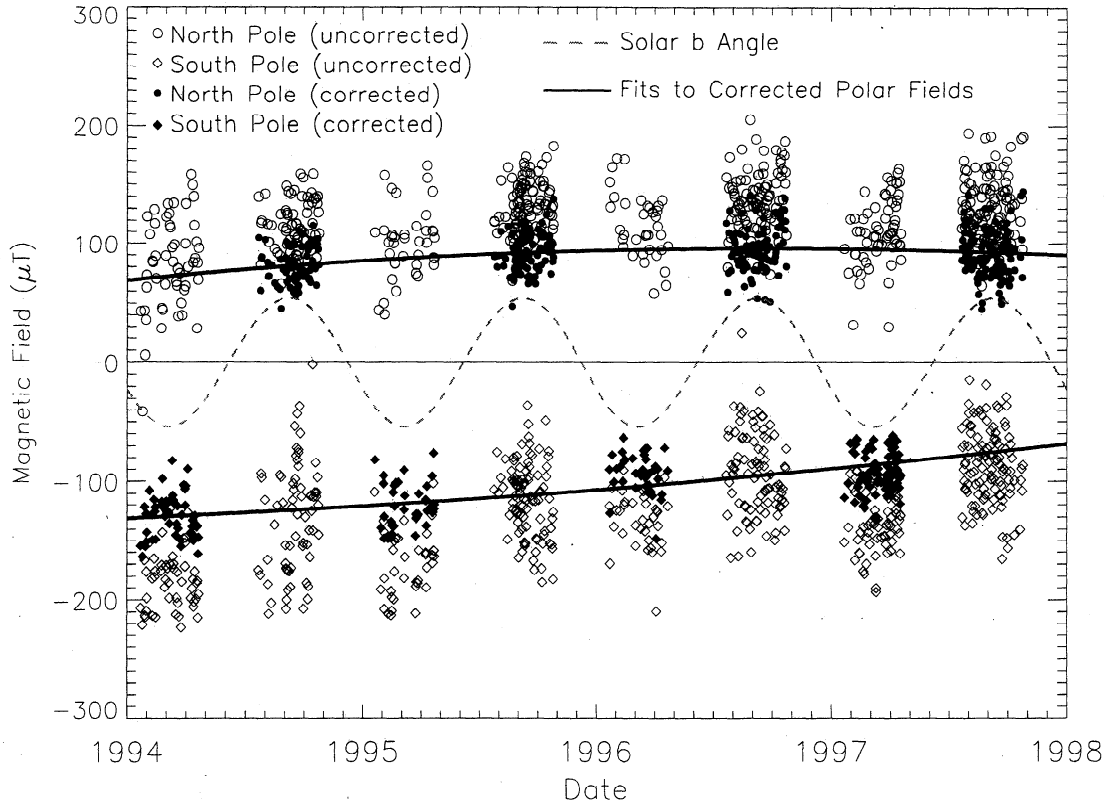

Figure 3. Uncorrected (open circles and diamonds) and corrected (solid circles and diamonds) average polar field strengths as a function of time (late 1993 to late 1997) for each WSO magnetogram having a solar b angle greater than | 5° |. (Only magnetic field measurements within 20° longitude of the Sun's central meridian, and in this plot, at sine latitudes of ± 14.5/15.0 were used to calculate the average polar field strengths.) When a particular hemisphere of the Sun is directed maximally toward the Earth, the spread in the uncorrected polar field values is larger in the hemisphere directed away from the Earth. The solid black curves are second-order polynomial fits to the most reliable data at each pole. Only those corrected polar field values used to make the polynomial curves are shown. The dashed gray sinusoidal line is the solar b angle as a function of time.

magnitudes and time variations. Figure 3 shows the fits to the most reliable corrected data located at sine latitudes ±14.5/15.0. The WSO magnetograms from early 1994 to late 1997 were used to construct the set of four polynomials. The average polar field strength at each polar latitude is normalized to the mean value predicted by the empirical fit, but the standard deviation is preserved.

Between sine latitudes +12.5/15.0 and -12.5/15.0 the solar magnetic field is usually measured reliably. As a result, we simply multiply each magnetic field measurement between these two latitudes by the appropriate trigonometric factor to remove north-south projection effects due to solar b angle only. The magnetograms are then assembled into synoptic maps. These synoptic maps have at this point been corrected for all longitudinal projection effects but must still be corrected for simple latitudinal projection effects (i.e., they must be divided by $\sin\theta$). This step is done just before the PFSS code is used.

3.4. Gaps in the Synoptic Maps

Inevitably, gaps arise in the synoptic maps. For full-rotation synoptic maps we fill large gaps with data from previous Carrington rotations as necessary. Smaller gaps (~15° wide in Carrington longitude or less) are filled by interpolation.

Gaps in daily updated maps must be treated differently. Large gaps are not filled at all, because a main objective of this study is to establish whether using the most recent magnetic observations improve solar wind predictions over the traditional approach (i.e., using the synoptic map from the last rotation to predict solar wind values for the next solar rotation). No predictions are made in such instances. If the gaps are "small" (a term difficult to define precisely), we fill them by interpolation. As shown in section 5, the greater the number of unfilled gaps, the poorer the model predictions. The ability to fill gaps in the synoptic maps from one observatory with observations from another would be thus extremely useful.

4. Modifications to the Wang-Sheeley Model

As mentioned in section 2, we have made two significant changes to the published version of the WS model. The changes occur after the PFSS model is applied to the input data and involve (1) the use of an empirical function to relate expansion factor with velocity and (2) the manner in which the solar wind is propagated out to Earth.

We apply the PFSS model using a standard approach. We set the source surface radius to $R_s = 2.5\ R_\odot$ [*Altschuler and Newkirk*, 1969; *Hoeksema*, 1983; and *Wang and Sheeley*, 1990] and obtain the radial potential field solution of the corona in terms of a series expansion of spherical harmonics [*Altschuler and Newkirk*, 1969; *Wang and Sheeley*, 1992]. We truncate the series above multipole $\ell = 30$.

4.1. Expansion Factor-Velocity Relationship

The magnetic expansion factors f_s are determined at each point P on the source surface by comparing the computed local field strength $B^P(R_s)$ at P with the associated photospheric value $B^P(R_\odot)$, as tracked back along the field line passing through P. Mathematically, $f_s = (R_\odot/R_s)^2 \left[B^P(R_\odot)/B^P(R_s)\right]$. Once all the expansion factors are determined, the solar wind speed is assigned to each point on the source surface by using the following empirical relationship between solar wind velocity and expansion factor:

$$v\,(f_s) = 267.5 + \left[410/(f_s)^{2/5}\right]. \qquad (4)$$

This equation applies strictly near the solar equator, since it was derived from low latitude in situ data. We note here an important difference between our approach and that of *Wang and Sheeley* [1990, 1992]. Their $v - f_s$ relationship is based upon the empirical correlation found between the solar wind velocities observed at Earth with the corresponding f_s values determined at the source surface. These two quantities are linked by the time required for the radially propagating solar wind (assumed to be flowing at constant velocity) to traverse from Sun to Earth.

In our implementation, however, the $v(f_s)$ function relates the expansion factor at the source surface with the solar wind velocity at the source surface. Our $v - f_s$ relationship is determined empirically, by iteration, until a reasonably good agreement between observed and predicted velocities at Earth is obtained. The assumption of constant flow speed partially explains why the WS $v - f_s$ plots [e.g., *Wang and Sheeley*, 1995b; *Wang et al.*, 1996] show so much scatter: solar wind streams do not travel with constant speeds and they interact with each other. Solar transients, e.g., coronal mass ejections (CMEs), are another reason the WS $v - f_s$ plots have so much scatter. The WS model predicts only the background flow, and CMEs were not excluded from the data sample.

4.2. Propagation of the Solar Wind to Earth

While more sophisticated numerical models exist to propagate solar wind from the Sun to Earth and to account for stream-stream interactions [e.g., *Hakamada and Akasofu*, 1982; *Pizzo*, 1982], a simpler method is used here.

In the inertial reference frame, the solar wind flows radially outward from the Sun. The synodic rotation period of the Sun (27.2753 days) is only slightly longer than the sidereal rotation period (25.4 days). Because of the small time difference between these two rotation periods and the resolution limit (i.e., 5°) set by the grid's finite cell size, we apply no corrections in the

arrival times of solar wind streams due to the motion of the Earth.

The first step in predicting the solar wind speed at Earth is to generate a solar wind speed synoptic map (for the source surface) using the method described in section 4.1 for converting f_s into velocity. Next, we record the time of central meridian passage and the associated velocity for each 5° × 5° cell on this map lying along the ecliptic line (i.e., the track of the subearth point). We propagate this time series of solar wind velocities outward toward Earth, allowing for interactions between the elements along the way. Each element is permitted to travel unhindered for 1/8 AU at a constant velocity equal to its assigned value at the source surface. The velocities of adjacent, interacting fluid elements are recalculated at the advanced position using the following weighting function:

$$v_i = \sqrt{\frac{2}{(1/v_i^2) + (1/v_{i+1}^2)}}. \quad (5)$$

The date of arrival of the faster moving element at 1/8 AU is adjusted to equal the date of arrival of the slower moving element. The velocities assigned to each element at 1/8 AU are now used, and this process is repeated out to 2/8 AU, and so on, out to 1 AU. The velocity time series at this point corresponds to the predicted solar wind speed at 1 AU for each new synoptic map. Because 72 velocity cells lie along the ecliptic line, we can predict the solar wind speed with a time resolution of ~1/3 day. Thus a 4-day advanced prediction means, in practical terms, that we select those two or three velocity values that lie within the time range 4 ± 0.5 days ahead of the date in which the synoptic map was created.

IMF polarity is predicted using nearly the same procedure except that we take the average of overlapping IMF elements instead of using a weighting function like (5). The average is used because the model is useful for predicting only the polarity and not the magnitude of the IMF at Earth. However, IMF polarity is assigned to the magnetic field values only after they have arrived at Earth.

Although we make 1- to 7-day advanced predictions each day using the daily updated and full-rotation synoptic maps, we present in this paper only the results for the 4-day advanced predictions. The 4-day advanced predictions provide the best overall agreement with the observations, because the mean propagation time from the source surface to Earth is ~4 days.

The procedures for making solar wind speed and IMF polarity predictions differ slightly when using daily updated as opposed to full-rotation maps. In the daily updated mode a new synoptic map is made each time a new WSO magnetogram is obtained. Using this new synoptic map, we make predictions 1- to 7-days in advance of the date the synoptic map was created (T_{newmap}). If a new magnetogram is obtained the next day, we generate a new synoptic map and make new 1- to 7-day advanced predictions based on it. If no magnetogram is available for the next day, we use the previous day's map, assign it a creation date of $T_{\text{newmap}} + 1$, and make solar wind predictions 1-7 days in advance of this new date. We continue this procedure until a new magnetogram becomes available or 7 days has passed. If a new magnetogram is not obtained within 7 days, we stop making predictions altogether.

The procedure followed for the full-rotation maps is simpler. Starting on the date for which a new Carrington rotation begins, the previous Carrington rotation's synoptic map is used to make 1- to 7-day advanced predictions. The same map is used for 28 days without being updated.

5. Predictions Using Three Methods

Using a 3-year (late 1994 to late 1997) set of WSO magnetograms, we predict the solar wind speed and IMF polarity using three different methods: the full-rotation (FR) method, the daily updated (DU) method, and the modified daily updated (MDU) method. The FR method uses a traditional approach, where solar wind predictions for a given Carrington rotation (CR) are based on the synoptic chart from the previous rotation. In the DU method the synoptic maps are updated daily with new magnetograms, but no modifications or corrections are made to the individual magnetograms before they are added to the synoptic charts. The MDU method uses the same approach as the DU method except that corrections (as discussed in detail in section 3.3) are made to the individual magnetograms before they are assembled into synoptic maps. The solar wind speed and IMF polarity predictions produced by the different prediction methods are compared with hourly averaged WIND satellite data from the same 3-year period.

5.1. Instructive Examples

Before presenting the results of the 3-year verification study, we introduce the methods used to compare the predictions with the observations. To clarify issues affecting the statistics and their meaning, we discuss two specific Carrington rotations in detail: CR 1899 and CR 1911.

5.1.1. Comparison of predicted and observed velocities: CR 1899 and CR 1911. In Figure 4, 4-day-advanced solar wind speed predictions from the three prediction methods are compared with WIND spacecraft velocity observations for CR 1899. Also shown are estimates of the uncertainty in the solar wind speed predictions, which are determined by calculating the predicted solar wind speeds for the expansion factors located 2.5° above and below each subearth point. To compare the predicted and observed velocities statistically, we reaverage the hourly averaged WIND satellite observations over 0.39-day (~9-hour) time intervals

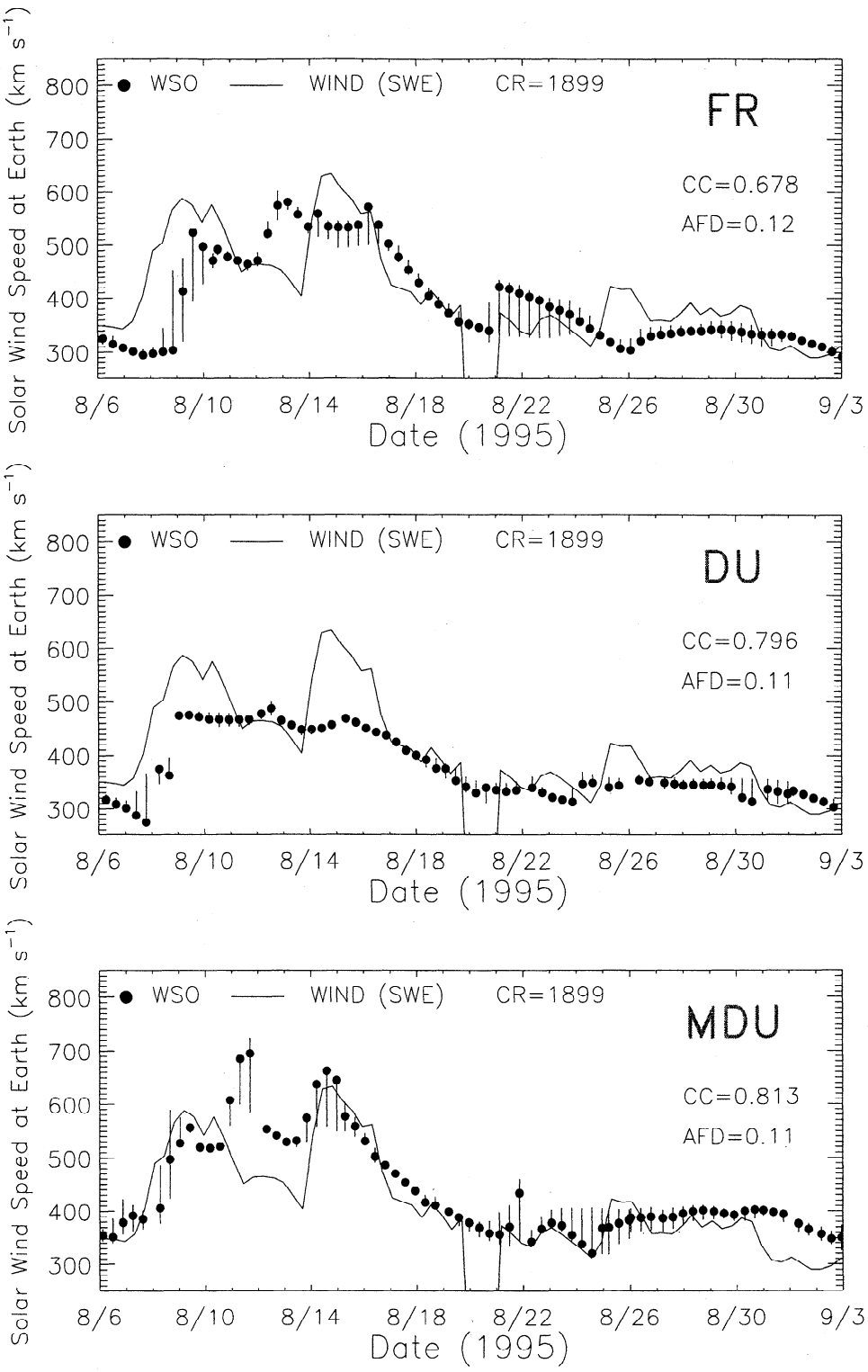

Figure 4. Comparison of the full rotation (FR), daily updated (DU), and modified daily updated (MDU) 4-day-advanced solar wind speed predictions (solid black circles) with 9-hour-averaged WIND satellite velocity observations (solid black lines) for Carrington rotation 1899. The vertical bars are estimates of the uncertainties in the solar wind speed predictions, which are determined by calculating the predicted solar wind speeds for the expansion factors located 2.5° above and below the subearth points.

centered about the predicted velocities, to match the effective temporal resolution of the input synoptic data. For CR 1899 the observed versus predicted correlation coefficients (CCs) for the FR, DU, and MDU methods are 0.678, 0.796, and 0.813, respectively. To quantify the statistical significance of these correlation coefficients, we calculate the probability of chance occurrence. When such a probability is less than 5%, the cor-

relation coefficient is considered significant, and when it is less than 1%, it is considered highly significant [*Taylor*, 1982]. However, solar wind streams persist, on average, for a minimum of 2 days [*Gosling et. al.*, 1972]. This must be taken into account to avoid erroneous confidence values. Because there are about 5.28 predicted data points in a 2-day interval, we divide each sample size by this number before making the above probability calculations. With persistence taken into account, the probability that any of the correlation coefficients listed above occurred by chance is less than 1%.

Another way to compare the observed v_o and predicted v_p velocities is to calculate the average fractional deviation (AFD) $\langle (v_p - v_o)/v_o \rangle$ during the 28-day time period shown in Figure 4. The AFDs for the FR, DU, and MDU methods are 0.12, 0.11, and 0.11, respectively. For a 400 km s^{-1} solar wind speed a 0.11-0.12 AFD corresponds to an average deviation of only ~45 km s^{-1}.

We compare in Figure 5 the results for the three prediction methods with the WIND satellite observations for CR 1911 (around the time of solar minimum).

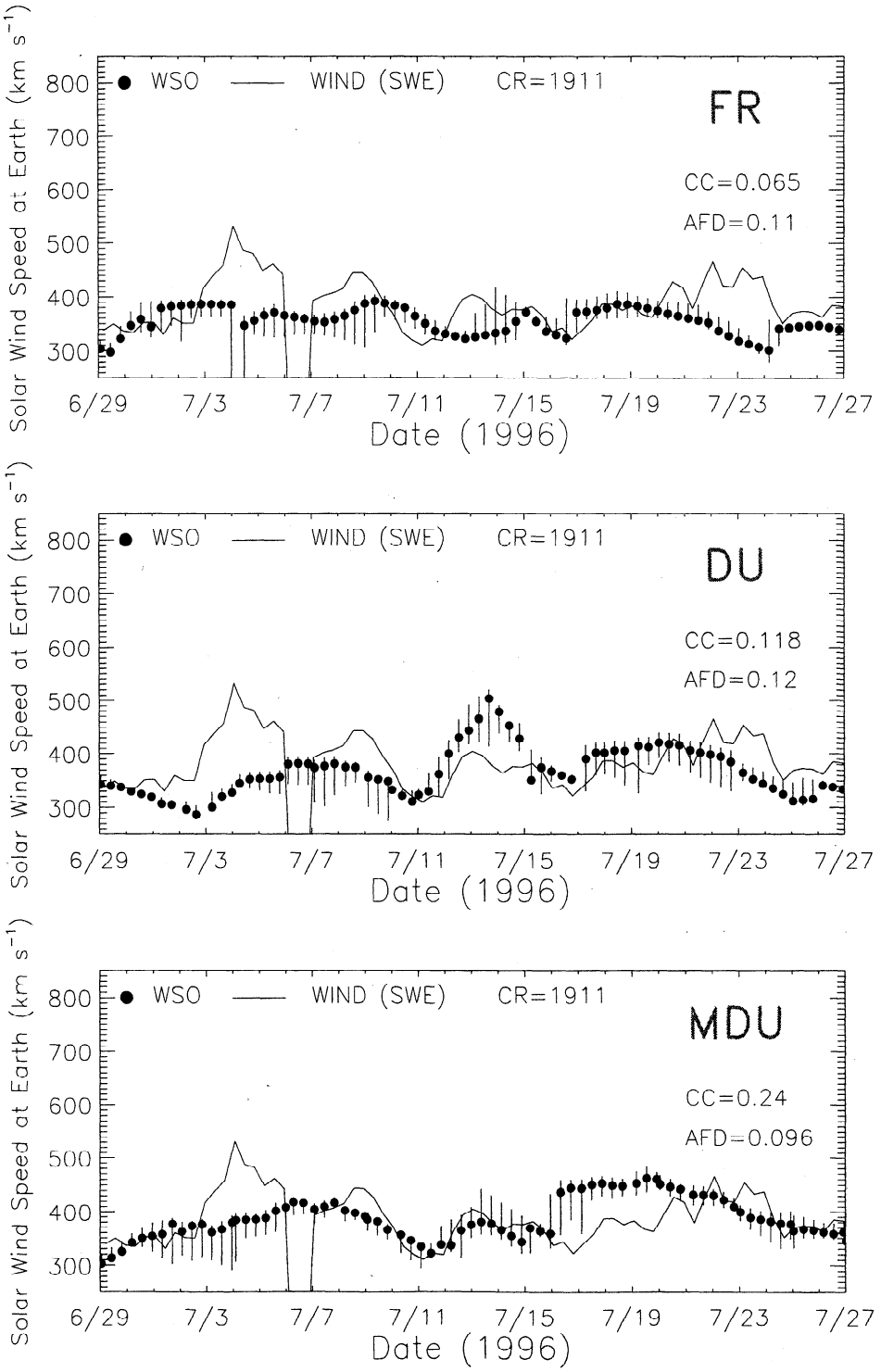

Figure 5. Similar to Figure 4, except for Carrington rotation 1911.

This figure is especially instructive because it highlights a number of the advantages and disadvantages of the three prediction methods. In the comparison between the WIND data and the FR method the CC is only 0.065. The probability of this correlation occurring by chance is very high, ~83%. However, the AFD is 0.11, indicating that the solar wind speed predictions are within roughly ±45 km s^{-1} of the observed values. During CR 1911 the solar wind speed is typically 400 km s^{-1} or less (i.e., mostly slow wind), and although the predictions are poorly correlated with the observations, the method correctly predicts generally slow wind velocity. Depending on one's predictive goal, the correlation coefficient is thus not always the best measure of the success or failure of the model.

The statistical comparison of the WIND data with the DU predictions yields a correlation coefficient of 0.118 and an AFD of 0.12. The probability of this correlation occurring by chance is ~69%. Statistically, both the FR and DU methods perform similarly. However, considering the flat dipole configuration of the Sun's global magnetic field during solar minimum, neither method is expected to perform significantly better than the other during this part of the solar cycle. Further into the solar cycle, we expect and see (section 5.2) that the daily updating methods tend to do better than the FR method.

The DU method also exhibits a "false alarm" prediction (i.e., a high wind speed prediction that does not take place) around July 13-14, 1996. Although the DU method updates the synoptic maps with new magnetograms daily, evaluations of the quality of the individual magnetograms are not performed before they are added to the maps. The last magnetogram added to the synoptic map before the abrupt increase in the predicted velocity appears is shown in Figure 2, our example of a very bad magnetogram. When this particular magnetogram is excluded from the synoptic maps, the false prediction disappears, even if no other corrections are made to the individual magnetograms. The reason that this false alarm occurs in the DU method and not in the FR method relates to differences in synoptic map construction. As seen in Figure 2, the quality of the measurements at the extreme eastern and western edges of this magnetogram is very poor. In the DU method the eastern edge of this magnetogram forms the leading edge of the new daily updated synoptic map. As mentioned in section 3.2, the eastern 10°-15° portion of daily updated synoptic maps often consists of observations from only one magnetogram, in this case a magnetogram of very poor quality. Synoptic FR maps are much less dependent upon individual magnetograms, because each region is composed of the weighted mean of many magnetograms, including the more reliable and heavily weighted measurements near central meridian.

In the comparison of the MDU predictions and WIND observations in Figure 5, qualitatively, the MDU method appears to fit the observations best. While the correlation coefficient for the MDU method is only 0.24, the AFD is 0.096. The probability of chance occurrence is ~40%. The false alarm prediction seen in the DU method has disappeared, and the MDU predictions between July 11-15, 1996, are now quite good.

The examples discussed in Figures 4 and 5 demonstrate the degree to which the predictions can be improved when (1) the synoptic maps are updated with new data as frequently as possible and (2) problematic effects are taken into account in the construction of the synoptic maps.

5.1.2. Comparison of predicted and observed IMF polarities for CR 1911. In Figure 6, we compare IMF polarity predictions with WIND satellite observations for CR 1911. The 9-hour-averaged WIND IMF values are normalized to equal unit value; a positive (negative) polarity indicates that the IMF is directed radially outward (inward) from the Sun to the Earth. The upright and upside-down gray triangles represent, respectively, the polarity predictions using the expansion factors 2.5° above and below the subearth points. Like the "error" bars seen in Figures 4 and 5, they assist in evaluating the reliability of the polarity predictions. Each 9-hour interval of WIND data corresponds to nine individual (hourly averaged) values when there are no gaps in coverage. If two thirds of the nine values have positive (negative) signs, they are assigned a polarity of +1 (-1). If less than two-thirds are of a particular sign, we assign that time interval a polarity of zero, implying mixed or indeterminate polarity.

To evaluate the statistical performance of the IMF polarity predictions, we calculate the fraction of correct polarity predictions (FCPP), excluding periods where the WIND data show mixed polarity. The FCPPs for the FR, DU, MDU methods over the 28-day period shown in Figure 6 are, respectively, 0.86, 0.91, and 0.86. Just as in the velocity predictions, persistence of the IMF must be taken into account before it can be established whether a particular FCPP value has statistical significance. We address the issue of persistence of the solar IMF in more detail in section 5.2.3.

5.2. Long-Term Evaluation of the Three Prediction Methods

A statistical comparison between the velocity and IMF polarity predictions of each scheme and the corresponding WIND satellite observations is displayed in Figure 7. Figures 7a and 7b show the comparison between the predicted and observed velocities using the average fractional deviation (AFD) and the correlation coefficient (CC), respectively. Figure 7c displays the FCPP achieved by each prediction scheme. Each symbol represents the statistical comparison between model predictions and the WIND satellite data for a temporal bin spanning three full Carrington rotations. The bin is stepped forward, in increments of one Carrington rotation, through the entire 3-year data set; the center of the bin is always placed at the start date of each new Car-

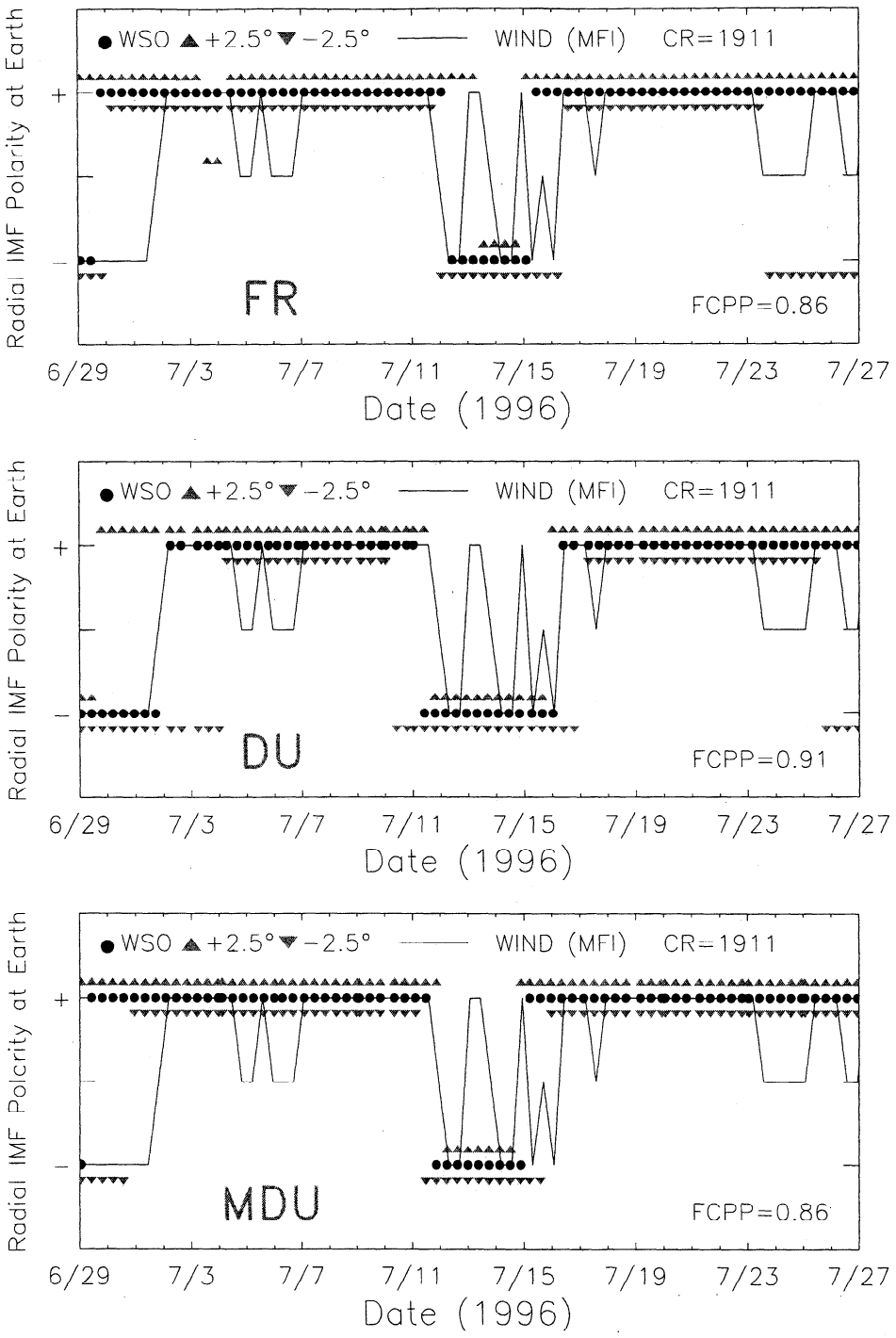

Figure 6. Comparison of the FR, DU, and MDU 4-day-advanced IMF polarity predictions (solid black circles) with WIND satellite observations (solid black line) for Carrington rotation 1911. The 9-hour-averaged WIND IMF values are normalized to equal unit value. A positive (negative) polarity indicates that the IMF is directed radially outward (inward) from the Sun to the Earth. The upright and upside-down gray triangles represent, respectively, the polarity predictions using the expansion factors 2.5° above and below the subearth points. Similar to the vertical bars seen for the velocity predictions, they assistant in evaluating the reliability of the polarity predictions.

rington rotation. For example, the bin centered about the start of CR 1891 begins at CR 1889.5 and ends at CR 1892.5. Thirty-seven comparison bins are thus produced. When there are no data gaps, each bin typically contains more than 200 individual predictions.

As discussed in the next two sections, at least five factors can hinder the performance of the different prediction methods: data gaps, transient events, the inclination of the ecliptic plane to the current sheet, the quality of the individual measurements (e.g., polar field mea-

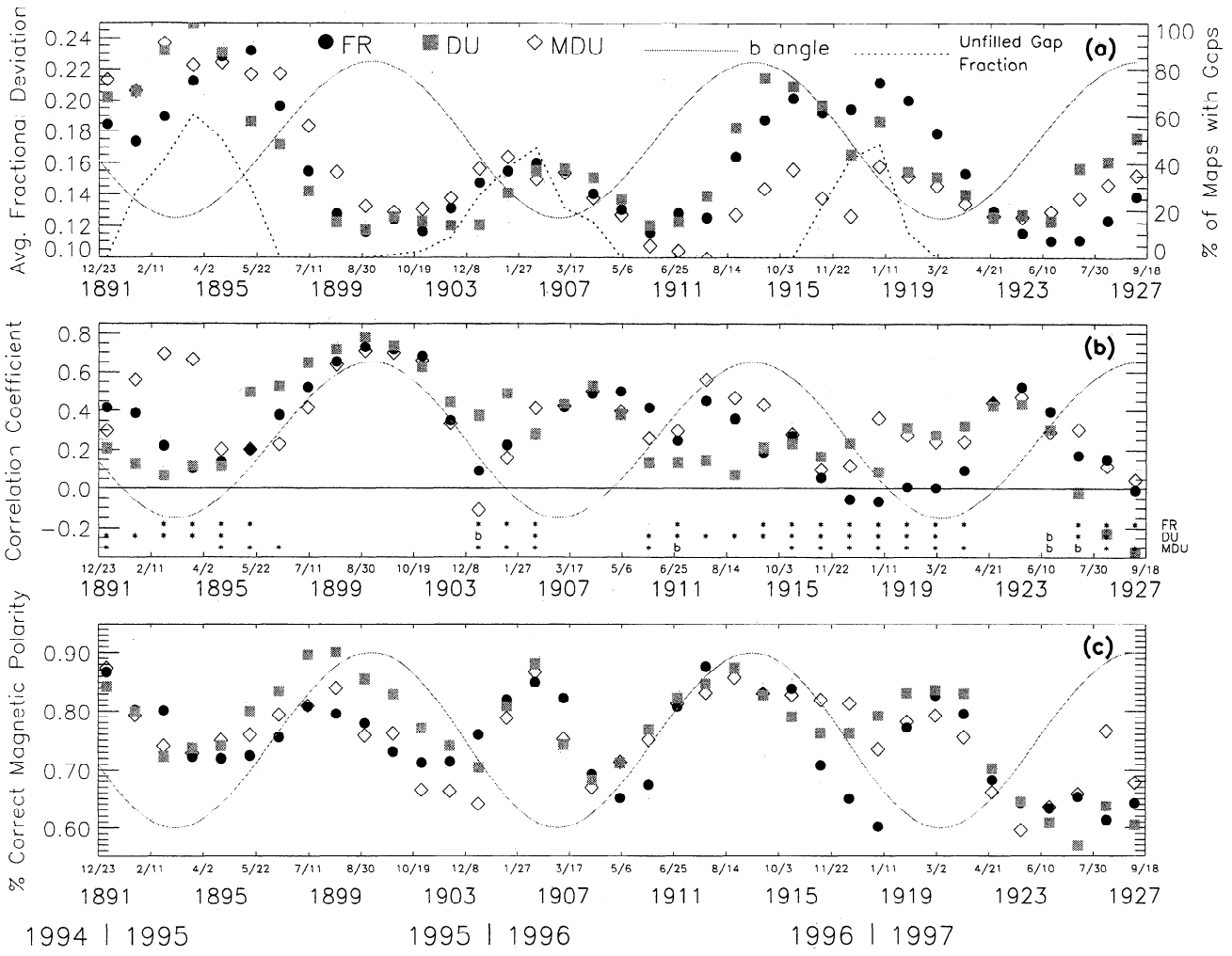

Figure 7. Comparison of the FR (solid black circles), DU (solid gray squares), and MDU (open diamonds) prediction schemes over the entire 3-year data set. The tick marks on the horizontal axis are 50-day time intervals. Each symbol represents the statistical comparison between model predictions and the WIND satellite data for a temporal bin spanning three full Carrington rotations. The temporal bins are centered at the beginning of each new Carrington rotation number (i.e., the large black numbers at the bottom of the plot, ranging from 1891 to 1927). (a,b) Statistical comparison between the predicted and observed velocities using, respectively, the average fraction deviation and the correlation coefficient. The dashed black line (Figure 7a) is the fraction of synoptic maps that have unfilled gaps in each bin for the DU method. The solid gray sinusoidal lines are the solar b angle. Correlation coefficients with a probability of chance occurrence greater than 5% are indicated at the bottom of the plot with either a "b" (i.e., borderline case) if the probability lies between 5 and 8% or an asterisk if the probability is greater than 8%. (c) Fraction of correct IMF polarity predictions for each method.

surements), and the rate of change of the global magnetic field configuration. While the prediction methods are equally sensitive to the first two factors, their sensitivities differ for the remaining three.

In the following comparison, we have done nothing to account for transient events (e.g., CMEs), which the WS model cannot predict. Thus the results presented below provide only a lower limit to the actual statistical agreement between the model's solar wind predictions and the "true" solar wind background parameters. In section 5.2.2, we discuss a particular case where the poor performance of the model can be directly linked to the occurrence of halo CMEs.

5.2.1. Comparing the predicted and observed velocities: Average fractional deviation. In Figure 7a, we see that the AFD fluctuates over a range of ~0.15 for all three methods during the 3-year comparison period. The dashed black line in Figure 7a represents the fraction of daily updated synoptic maps (i.e., created using the DU method) that have unfilled gaps in each of the time bins. The largest AFD values occur during approximately the first 6 months of the 3-year comparison period, when the unfilled gap fractions are particularly large. There are two additional periods when the unfilled gap fractions are significant (October 1995 to April 1996 and October 1996 to February 1997)

and the AFDs are correspondingly large. Clearly, all three prediction methods are sensitive to data gaps.

Data gaps do not explain all the large AFDs. There are two periods when the AFDs are large but the unfilled gap fractions are either very small or zero: August-October 1996 and July-September 1997. The first occurred during the 1996 solar minimum when the current sheet had a flat dipole configuration and the solar b angle was large. When the current sheet is nearly parallel to the ecliptic plane, reliable solar wind speed predictions depend acutely upon accurate knowledge of the current sheet's location. As discussed previously, the PFSS model, and therefore the location of the current sheet, is sensitive to the field strengths near the Sun's poles. As the magnitude of the solar b angle gets large, the magnetic field measurements of one of the Sun's polar fields become increasingly uncertain. In Figure 7a, we note an overall correlation between large b angle and large AFD from about CR 1905 onward (i.e., when the current sheet becomes mostly flat). During August-October 1996 the MDU method, with its polar field corrections, has significantly smaller AFDs than either the FR or the DU method. We conclude that inaccurate polar field measurements in combination with a flat current sheet result in less reliable solar wind speed predictions and thus larger AFDs. However, as seen in the MDU method, the predictions can often be improved when polar field corrections are made to the magnetograms. During the second time interval (July-September 1997), b is once again large and positive, but the FR method actually has smaller AFDs than either the MDU or DU methods. The current sheet began to deviate from its previously flat configuration by ~CR 1925-1926, decreasing the sensitivity of the models to uncertainties in the polar field strengths and explaining why the DU method has AFDs similar to those of the MDU method during the second time interval. The FR method makes the best predictions when the global solar magnetic field is changing slowly (recall that the FR prediction method updates the synoptic maps only once per Carrington rotation), which may explain why its AFDs are significantly smaller during CR 1925-1927.

Using the AFD as our criterion, we find the MDU method has the best overall performance of the three predictions methods. The AFDs for the complete 3-year study period are 0.159, 0.157, and 0.150 for the FR, DU, and MDU methods, respectively. Except for the first 6 months of the study, where the unfilled gap fraction is quite large and all the prediction methods suffer, the MDU method yields AFD values that consistently range between ~0.10 and ~0.15. For a typical solar wind speed of 400 km s^{-1}, an AFD ranging between 0.10 and 0.15 implies solar wind speed predictions that are, on average, within 40 to 60 km s^{-1} of the measured values.

5.2.2. Comparing the predicted and observed velocities: Correlation coefficient. For each prediction technique, we display in Figure 7b the 37 CCs produced by our sliding time bin comparison of predicted and observed velocities. Correlation coefficients with a probability of chance occurrence greater than 5% are indicated at the bottom of the plot with either a "b" (i.e., borderline case) if the probability lies between 5 and 8% or an asterisk if the probability is greater than 8%. Correlation coefficients that are statistically significant have blank entries at the bottom of the plot.

Time bins with statistically insignificant CCs tend to group around periods when the unfilled gap fraction is large. This is especially true for the MDU method even though it relies on the least data of the three methods; it is the only method that excludes poor quality data. (Recall that the unfilled gap fraction plotted in Figure 7a is for the DU method; the unfilled gap fractions for the MDU method are somewhat more extensive than those of the DU method because data are excluded.) This is consistent with the result from section 5.2.1, which found that the AFDs tend to be larger when the unfilled gap fraction is also large. Data gaps are one of the leading causes for the breakdown of the model.

Although large CCs and small AFDs are the statistical ideal (e.g., CR 1899), it is much more important, for forecasting purposes, that the model produce small AFDs (e.g., CR 1911) than large CCs, because the difference between fast and slow solar wind speeds is better distinguished. For example, consider time interval CR 1892-CR 1894, which has both large CCs and AFDs for the MDU method. The large CCs imply that the predictions track the changes in the observed velocities well, but the large AFDs suggest uncertainties in the predicted velocities of the order of ~100 km s^{-1} for a 400 km s^{-1} solar wind. Such large uncertainty makes it difficult to distinguish between fast (~500 km s^{-1}) and slow (~300 km s^{-1}) wind.

The MDU method significantly outperforms both the DU and FR methods during the period following solar minimum (May 1996) until about October 1996, when the unfilled gap fraction becomes large. As mentioned in the previous section, the combination of a flat current sheet and a large solar b angle explains why the MDU method, with its polar field corrections, does better than the other two methods during this time interval.

The number of coronal mass ejections (CMEs) generated during the first 10 months of 1997 (e.g., 13 halo events occurred) is much greater than that for the whole of 1996 (only two halo events) as seen in the Large Angle and Spectrometric Coronograph (LASCO) Experiment CME List (http://ares.nrl.navy.mil/cmelist.html). This may partially explain some of the statistically insignificant CCs for the year 1997. In fact, three halo CMEs occurred during a 30-day period spanning CR 1926 and CR 1927 when the solar b angle was large and all three models did particularly poorly.

For each prediction method, over the complete 3-year set of data, the CCs are as follows: MDU method, 0.389; DU method, 0.363; and the FR method, 0.343. With typically more than 2200 comparisons (corresponding to an equivalent sample number of $2200/5.28 \approx 417$) be-

tween predictions and observations for each method, the probability that any of these CCs occurred by chance is many orders of magnitude less than 1%.

5.2.3. Comparing the predicted and observed IMF polarities. We compare each model's IMF polarity predictions with WIND satellite observations by calculating the fraction of correct polarity predictions (FCPP). In Figure 7c, we use our sliding time bin technique to calculate the FCPP for each bin and for each prediction method.

There is an overall tendency for the FCPP values to be large when the magnitude of the solar b angle is also large. This trend makes sense physically, because the low inclination of the current sheet to the ecliptic plane during most of this 3-year period makes predicting the time of current sheet crossing difficult. A large solar b angle is more likely to place the subearth point clearly above or below the solar current sheet, thus minimizing the likelihood of crossing.

The FCPPs for the entire 3-year study period are 0.764, 0.746, and 0.751 for the DU, FR, and MDU methods, respectively. To establish the statistical significance of these results, we must first account for persistence in the IMF polarity. We make the simple, but very conservative, assumption that the Sun's global magnetic field was, on average, that of a tilted dipole during the entire 3-year study period. Hence the persistence of the solar wind is expected to be 13.64 days (i.e., half of a Carrington rotation) for each IMF polarity. We then divide the IMF sample number for each prediction method by this time period to account for persistence. The resulting sample sizes are, respectively, 174, 145, and 145 for the DU, FR, and MDU methods. We expect an FCPP of 50%, if the probability of obtaining a particular IMF polarity is due only to that of random chance. Using binomial statistics [*Taylor*, 1982], we calculate the probability of obtaining an FCPP greater than or equal to that actually achieved purely as a result of chance. For each prediction method, this probability is many orders of magnitude less than 1%.

The flat dipole configuration of the global solar magnetic field during solar minimum, and the lack of sensitivity of the source-surface field to small-scale field changes at the photosphere is the likely explanation for the very similar performances of the three prediction methods. As the solar cycle progresses and the current sheet warping increases to greater degrees, the models are likely to begin to differ more from each other in their IMF polarity predictions.

6. Summary and Conclusions

We have made a number of changes to both the original WS model prediction scheme and to its input (i.e., WSO magnetograms). With these changes we have conducted a statistical comparison between a traditional version and two daily updated versions of the WS model using 3 years (late 1994-late 1997) of WIND satellite data as a baseline. Our results show that the inverse $v - f_s$ correlation is valid on a timescale of the order of a day and that the MDU method in particular shows a clear improvement over the more traditional FR prediction method.

The original WS model/prediction technique is modified in two ways. First, we use a continuous empirical function to relate expansion factor with velocity, assigning the velocities at the source surface instead of at Earth. Second, we propagate radially the flow out to Earth using a simple scheme which includes the effect of solar wind stream interactions. The model input is modified to account for a number of problematic factors including projection effects, annual variation in the solar b angle, poor polar field determinations, and quality control of the individual magnetograms. We find that when these factors are carefully accounted for, the performance of the model is greatly improved. The input data are also modified by updating the synoptic maps daily, when possible. This allows the model to keep pace with changes in the global solar magnetic field configuration on a timescale of the order 1 day. Solar and Heliospheric Observatory/Michelson Doppler Imager (SOHO/MDI) and Global Oscillation Network Group (GONG) magnetograms are well suited for updating on shorter time scales.

The model can break down for a number of reasons. During intervals when the unfilled gap fraction is large, the velocity predictions tend to have large AFDs and to be statistically uncorrelated with the observations. In addition, the PFSS model is sensitive to field strengths near the Sun's poles. When the solar b angle is large and the current sheet flat, the performance of the models is diminished. The predictive performance of the DU method is most affected on such occasions, while the MDU method (with its polar field corrections) is least affected. False alarm predictions are more likely to occur when b is large. Finally, an increase in the number of CMEs (which the models cannot predict) generated near the end of the 3-year study period (especially during CR 1926 and CR 1927), combined with a large solar b angle, contribute to the poor performance of the models at this time.

We find that the MDU method with its polar field corrections and data quality control technique offers the best background velocity predictions of the three methods. The MDU prediction method has the most consistent AFD values, which varied between 0.10 and 0.15 for most of the 3-year study period. That is, the MDU method can (on average) reliably predict the solar wind speed to within 10-15%, thus making it easier to distinguish between fast and slow streams. Of the three prediction methods the MDU method has the largest correlation coefficient (0.389) between solar wind speed predictions and observations. We find that all three methods predict, on average, the solar wind IMF polarity correctly ~75% of the time. When the Sun's magnetic dipole current sheet is flat, all three models

predict the IMF polarity best when the subearth point is located far above or below the current sheet. When the current sheet begins to warp as the solar cycle progresses, the predictive performances of the models with respect to the IMF are likely to differ.

In addition to improving forecasts of current sheet crossing times and the occurrence, arrival times, and velocities of high-speed streams, reliable velocity and IMF polarity predictions can be used in other space weather applications. For instance, velocity and IMF polarity predictions can be used to forecast the geomagnetic *Ap* index [*Detman and Vassiliadis*, 1997]. Improved predictions of solar wind ambient conditions can provide kinematic and magnetohydrodynamic solar wind models with more realistic boundary conditions. Eventually, this could lead to improved forecasts of the arrival time, structure, and geoeffectiveness of transients events such as CMEs.

Acknowledgments. We thank Y.-M. Wang and N. R. Sheeley for their periodic assistance with this project and for providing us with their PFSS code. We thank Wilcox Solar Observatory for access to their daily magnetograms. We consulted with J. T. Hoeksema on the techniques used at WSO for constructing synoptic maps from individual magnetograms. His assistance and advice are greatly appreciated. We thank Principal Investigator K. W. Ogilvie, and J. T. Steinberg and A. J. Lazarus for allowing us access to the SWE key parameter data. Principal Investigator R. P. Lepping, the MFI processing team, WIND, ISTP, and Goddard Space Flight Center are thanked for allowing us access to the MFI key parameter data. T. R. Detman placed the WIND-derived velocity and magnetic field data (generated from the NASA ISTP key parameter data) into the hourly averaged values used in this work. We appreciate his efforts. This work was funded by the Office of Naval Research under grant N00014-96-F-0193.

Janet G. Luhmann thanks Craig D. "Ghee" Fry and another referee for their assistance in evaluating this paper.

References

Altschuler, M. A., and G. Newkirk Jr., Magnetic fields and the structure of the solar corona, *Sol. Phys., 9,* 131-149, 1969.

Detman, T. R., and D. Vassiliadis, Review of techniques for magnetic storm forecasting, in *Magnetic Storms, Geophys. Monogr. Ser.,* vol. 98, edited by B. T. Tsurutani et al., pp. 253-266, AGU, Washington, D. C., 1997.

Fry, C. D., and S.-I. Akasofu, Latitudinal dependence of solar wind speed, *Planet. Space Sci., 35*(7), 913-920, 1987.

Gosling J. T., V. Pizzo, M. Neugebauer, and C. W. Snyder, Twenty-seven-day recurrences in the solar wind speed: Mariner 2, *J. Geophys. Res., 77,* 2744-2751, 1972.

Hakamada, K., and S.-I. Akasofu, Simulation of three-dimensional solar wind disturbances and resulting geomagnetic storms, *Space Sci. Rev., 31,* 3-70, 1982.

Hoeksema, J. T., J. M. Wilcox, and P. H. Scherrer, Structure of the heliospheric current sheet in the early portion of sunspot cycle 21, *J. Geophys. Res., 87,* 10,331-10,338, 1982.

Hoeksema, J. T., J. M. Wilcox, and P. H. Scherrer, The structure of the heliospheric current sheet: 1978-182, *J. Geophys. Res., 88,* 9910-9918, 1983.

Hoeksema, J. T., Structure and evolution of the large scale solar and heliospheric magnetic fields, Ph.D. thesis, 222 pp., Stanford Univ., Stanford, Calif., April 1984.

Levine, R. H., M. D. Altschuler, and J. W. Harvey, Solar sources of the interplanetary magnetic field and solar wind, *J. Geophys. Res., 82,* 1061-1065, 1977.

Nolte, J. T., A. S. Krieger, A. F. Timothy, R. E. Gold, E. C. Roelof, G. Vaiana, A. J. Lazarus, J. D. Sullivan, and P. S. McIntosh, Coronal holes as sources of solar wind, *Sol. Phys., 46,* 303-322, 1976.

Pizzo, V. J., A three-dimensional model of corotating streams in the solar wind 3. Magnetohydrodynamic streams, *J. Geophys. Res., 87,* 4374-4394, 1982.

Schatten, K. H., J. M. Wilcox, and N. F. Ness, A model of interplanetary and coronal magnetic fields, *Sol. Phys., 9,* 442-455, 1969.

Taylor, J. R. *An Introduction to Error Analysis; The Study of Uncertainties in Physical Measurement,* 270 pp., Univ. Sci. Books, Mill Valley, Calif., 1982.

Wang, Y.-M., and N. R. Sheeley, Solar wind speed and coronal flux-tube expansion, *Astrophys. J., 355,* 726-732, 1990.

Wang, Y.-M., and N. R. Sheeley, Why fast solar wind originates from slowly expanding coronal flux tubes, *Astrophys. J., 372,* L45-L48, 1991.

Wang, Y.-M., and N. R. Sheeley, On potential field models of the solar corona, *Astrophys. J., 392,* 310-319, 1992.

Wang, Y.-M., and N. R. Sheeley, Solar implications of ULYSSES interplanetary field measurements, *Astrophys. J., 447,* L143-L146, 1995a.

Wang, Y.-M., and N. R. Sheeley, Empirical relationship between the magnetic field and the mass and energy flux in the source regions of the solar wind, *Astrophys. J., 449,* L157-L160, 1995b.

Wang, Y.-M., S. H. Hawley, and N. R. Sheeley, The magnetic nature of coronal holes, *Science, 271,* 464-469, 1996.

Wintoft, P., and H. Lundstedt, Prediction of daily average solar wind velocity from solar magnetic field observations using hybrid intelligent systems, *Phys. Chem. Earth,* 22(7-8), 617, 1997.

Zhao, X., and J. T. Hoeksema, Unique determination of model coronal magnetic fields using photospheric observations, *Sol. Phys., 143,* 41-48, 1993.

Zhao, X., and J. T. Hoeksema, A coronal magnetic field model with horizontal volume currents, *Sol. Phys., 151,* 91-105, 1994.

Zhao, X., and J. T. Hoeksema, Prediction of the interplanetary magnetic field strength, *J. Geophys. Res., 100,* 19-33, 1995.

C. N. Arge, Cooperative Institute for Research in Environmental Sciences, University of Colorado and Space Environment Center, National Oceanic and Atmospheric Administration, Boulder, CO 80303. (narge@sec.noaa.gov)

V. J. Pizzo, Space Environment Center, National Oceanic and Atmospheric Administration, Boulder, CO 80303. (vpizzo@vulcan.sec.noaa.gov)

(Received July 19, 1999; revised November 3, 1999; accepted November 3, 1999.)